Cell

Systematic Identification of Molecular Subtype-Selective Vulnerabilities in Non-Small-Cell Lung Cancer

Hyun Seok Kim,[1] Saurabh Mendiratta,[1] Jiyeon Kim,[2] Chad Victor Pecot,[5] Jill E. Larsen,[3] Iryna Zubovych,[4] Bo Yeun Seo,[1] Jimi Kim,[1] Banu Eskiocak,[1] Hannah Chung,[1] Elizabeth McMillan,[1] Sherry Wu,[5] Jef De Brabander,[4] Kakajan Komurov,[7] Jason E. Toombs,[3] Shuguang Wei,[4] Michael Peyton,[3] Noelle Williams,[4] Adi F. Gazdar,[3] Bruce A. Posner,[4] Rolf A. Brekken,[3] Anil K. Sood,[6] Ralph J. Deberardinis,[2] Michael G. Roth,[4,8] John D. Minna,[3,8] and Michael A. White[1,8,*]

[1]Department of Cell Biology
[2]Children's Medical Center Research Institute
[3]Hamon Center for Therapeutic Oncology Research
[4]Department of Biochemistry
University of Texas Southwestern Medical Center, Dallas, TX 75390, USA
[5]Division of Cancer Medicine
[6]Center for RNA interference and Non-Coding RNA
University of Texas MD Anderson Cancer Center, Houston, TX 77030, USA
[7]Division of Biomedical Informatics, Cincinnati Children's Hospital Medical Center, Cincinnati, OH 45229, USA
[8]These authors contributed equally to this work
*Correspondence: michael.white@utsouthwestern.edu
http://dx.doi.org/10.1016/j.cell.2013.09.041

SUMMARY

Context-specific molecular vulnerabilities that arise during tumor evolution represent an attractive intervention target class. However, the frequency and diversity of somatic lesions detected among lung tumors can confound efforts to identify these targets. To confront this challenge, we have applied parallel screening of chemical and genetic perturbations within a panel of molecularly annotated NSCLC lines to identify intervention opportunities tightly linked to molecular response indicators predictive of target sensitivity. Anchoring this analysis on a matched tumor/normal cell model from a lung adenocarcinoma patient identified three distinct target/response-indicator pairings that are represented with significant frequencies (6%–16%) in the patient population. These include *NLRP3* mutation/inflammasome activation-dependent FLIP addiction, co-occurring *KRAS* and *LKB1* mutation-driven COPI addiction, and selective sensitivity to a synthetic indolotriazine that is specified by a seven-gene expression signature. Target efficacies were validated in vivo, and mechanism-of-action studies informed generalizable principles underpinning cancer cell biology.

INTRODUCTION

Widespread evidence indicates that aberrant cancer cell-regulatory frameworks generate collateral vulnerabilities that can be exploited for therapeutic benefit. These vulnerabilities can be a consequence of oncogene addiction, gene-specific haploinsufficiencies, and other genetically and epigenetically derived fragilities in cell-regulatory systems (Jänne et al., 2009; Luo et al., 2009; Muller et al., 2012). The critical barrier confronting this opportunity, for many tumor types, is the extreme heterogeneity of the molecular etiology of neoplastic disease, which confounds annotation of effective context-selective intervention targets. For non-small-cell lung cancer (NSCLC), a tumor responsible for 1 million deaths/year, over 160 nonsynomous somatic mutations are detected per tumor, and the vast majority of these mutations are nonrecurrent (Cancer Genome Atlas Research Network, 2012; Imielinski et al., 2012). Actionable mutations have been identified in epidermal growth factor receptor (EGFR) and EML4-ALK (Lynch et al., 2004; Soda et al., 2007) but are present in only 15% of lung adenocarcinomas (Imielinski et al., 2012), whereas the majority of NSCLC patients are not associated with any known pharmaceutically addressable target. This missing coverage underscores the need to develop new target opportunities that are tightly linked to molecular response indicators.

To generate a testbed representative of the molecular heterogeneity of NSCLC, we assembled a panel of 91 lung tumor-derived cell lines and 3 immortalized nontumorigenic airway epithelial cultures. Though limited by the sparse complexity of the tissue culture environment and therefore limited in the synthetic genetic and chemical interactions that can be observed, this cell-line panel has been shown to recapitulate genetic profiles found in tumors and to recapitulate selective responsiveness to molecularly targeted therapies (Gazdar et al., 2010; Sharma et al., 2010). Beginning with a matched tumor/normal cell model from a single lung adenocarcinoma patient, 230,000 synthetic small molecules and two independent whole-genome

arrayed small interfering RNA (siRNA) libraries were used to identify chemical and genetic perturbations selectively toxic to the patient's tumor cell line. These agents were then tested to identify perturbations that were innocuous to nontumorigenic cells but had activity in at least 30% of the NSCLC cell lines. The resulting toxicity patterns were correlated with genomic profiles to identify somatic mutations and expression signatures that predicted sensitivity or resistance to these perturbations. In this way, we identified three distinct target/response-indicator pairings. First, we found that NLRP3 mutations, which occur in 16% of lung adenocarcinomas, drive addiction to the antiapoptotic protein FLIP. The mechanism of action is through NLRP3-dependent chronic activation of inflammasome signaling, which sensitizes these cells to FLIP-dependent restraint of caspase-8-induced cell death. Second, we found that co-occurring mutations in KRAS and LKB1, present in 6% of lung adenocarcinoma patients, are sufficient to drive addiction to the coatomer complex I (COPI)-dependent lysosome acidification. This liability was determined to be a consequence of obligate supply of TCA-cycle substrates by lysosome-dependent consumption of extracellular macromolecules. Chemical inhibition of this process, with the natural product saliphenylhalamide A, inhibited $KRAS^{mut}/LKB1^{mut}$ tumor cell survival in vitro and in vivo. Finally, we found that selective sensitivity to a synthetic indolotriazine defines a subtype of NSCLC cells estimated to occur at a frequency of ~10% of lung tumors. Indolotriazine sensitivity corresponded to selective activation of an endoplasmic reticulum stress response and can be effectively predicted using a seven-gene quantitative mRNA expression signature.

RESULTS

Public and Private Vulnerabilities in NSCLC

To begin to assess the diversity of selective vulnerabilities that can arise within lung cancer cell-autonomous regulatory contexts, we selected a matched tumor/normal pair (HCC4017/HBEC30KT), derived from a 62-year-old female smoker with stage 1A adenocarcinoma, for extensive functional and genomic interrogation (Figure 1A). Authentic somatic mutations and copy number variation, in the tumor line as compared to normal cells, were identified from whole-exome hybridization-capture sequencing (130× average read-depth; Table S1 and Data S1 available online). Two hundred and ninety-six nonsynonymous exonic single-nucleotide somatic variants were detected in HCC4017 (Figure 1B), 152 of which are predicted to be deleterious to protein function (Data S1). Copy number variation was extensive, as estimated by exon read-depth (Figures 1B and S1A) and SNP array (Figure S1A), and correlated with relative mRNA concentrations as determined by RNA sequencing (RNA-seq) (Data S2; Figure S1A). Two whole-genome arrayed siRNA libraries and a collection of ~230,000 chemical compounds were then screened to identify agents selectively toxic to HCC4017 versus HBEC30KT (Data S2 and S3).

A Z score cutoff of −3 was used to identify candidate HCC4017-selective siRNA sensitivities. This thresholding resulted in predominantly nonoverlapping sets of candidates from each siRNA library, presumably due to a combination of false-negative and false-positive relationships. As previously described (Jacob et al., 2011), the former is at least partially an artifact of assigned selection thresholds. In direct support of this, the empirical cumulative distribution of the Z scores from siRNA pools in library 1, corresponding to "hits" from library 2, indicated a significant enrichment of activity as compared to the background distribution (Figure S1B). To defend against false positives, individual oligos were tested for each of the 326 nonredundant hits from the union of the two libraries together with a K-S statistic that predicts oligonucleotide seed sequence-specific activity that is independent of target depletion (Tables S2 and S3; Data S4). Eighty-five surviving siRNA pools that were reproduced in HCC4017 and also innocuous upon testing in HBEC30KT and two additional telomerase/*CDK4*-immortalized nontumorigenic HBEC lines were then examined across a panel of 21 additional NSCLC cell lines (Data S5; Figures 1C and S1C).

A striking feature of the response of the cell-line panel to the siRNA collection was the largely idiosyncratic activity pattern (Figure 1C). Forty percent of the tested siRNAs had measurable consequences on the viability of 10% or less of the cell-line panel, and no single siRNA pool was identified with activity in over 90% of the panel (Data S5; Figure 1C). Manual curation of the biological processes served by the siRNA target genes indicated an enrichment of signal transduction machinery and transcription factors within the "private" target class and an enrichment of housekeeping machines (cell-cycle control, mRNA splicing, ribosomal proteins, and vesicle trafficking) within the "public" target class (Data S6; Figure 1D). Among the private targets, small-molecule inhibition of USP8 (Guédat and Colland, 2007) largely recapitulated the selectivity of siRNA-mediated USP8 depletion, suggesting bona fide selectivity (Figure S1D). We found significant correlation of the private target class of HCC4017-sensitive siRNAs with low-target gene expression, suggesting that the private nature of some targets may be at least partially a consequence of expression bias (Figure S1E). As a whole, siRNA targets were recovered evenly from all genomic loci with the exception of homozygously deleted regions where, as expected, none were located (Figures 1B and S1F). However, a slightly larger number of hits (*CACNA2D4*, *POM121L12*, *TMEM106B*, *BZW2*, *RBBP9*, *HBA1*, *NUPL2*, *SDK1*, *VSTM2A*, *C16orf54*, and *CYC1*) were identified from amplified and overexpressed loci as compared to the rest of the genome (Figures S1F and S1G). A first-degree interaction network was constructed to identify potential coherent relationships among HCC4017-selective targets and the somatic mutations detected within that cell line (Figure S1H). Though verifiable and informative relationships were detected (Figures S1I and S1J), direct connections to somatic variation appear insufficient to account for the high frequency of private vulnerabilities identified within this cell line.

Context-Selective FLIP Addiction

We prioritized relationships found in at least 30% of the NSCLC panel to afford an opportunity for codetection of genetic response indicators. Depletion of *CFLAR*, which encodes the catalytically inactive caspase-8 analog FLIP (Irmler et al., 1997), was sufficient to markedly induce apoptosis in HCC4017 cells and was toxic to multiple additional NSCLC lines as compared

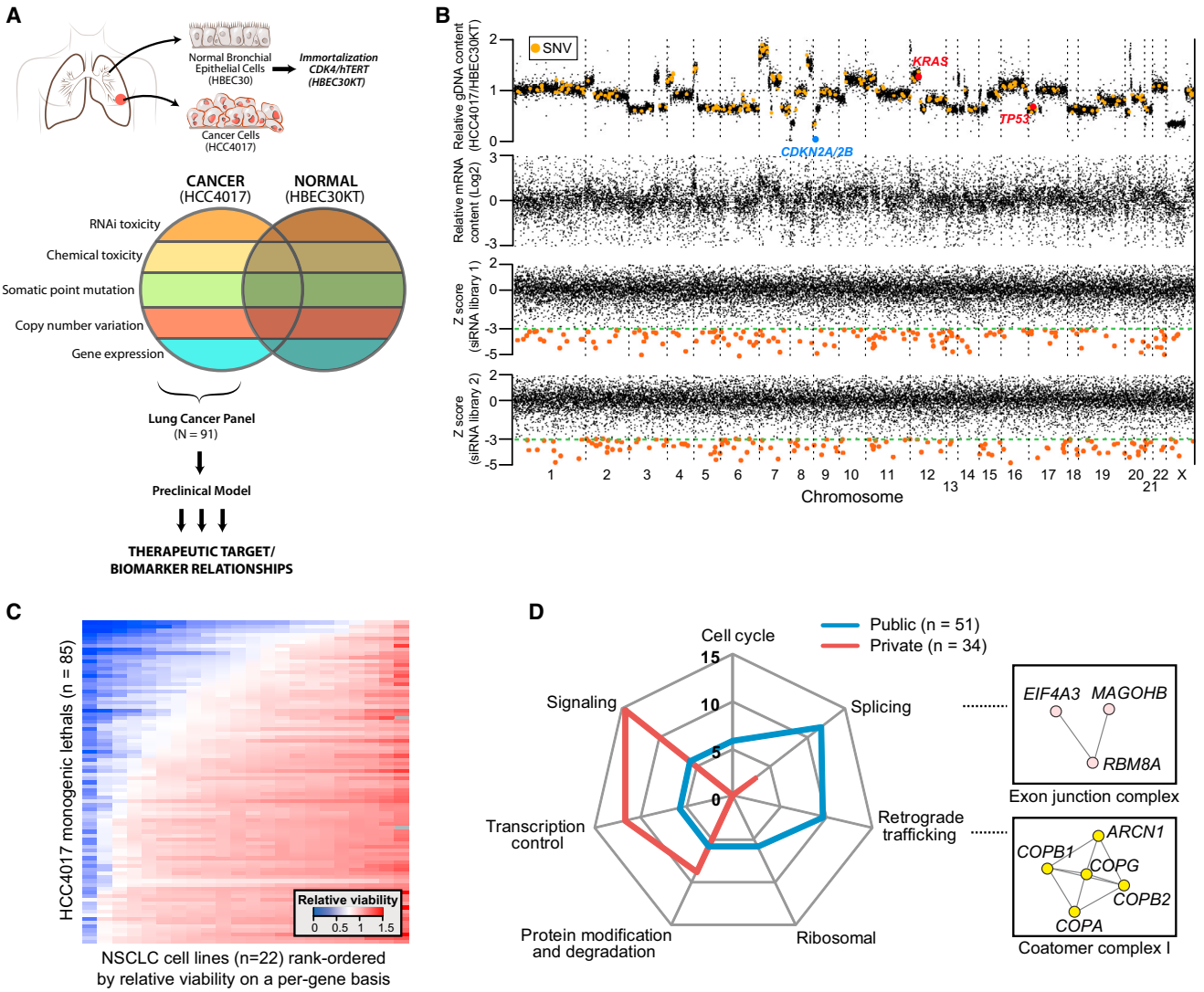

Figure 1. Public and Private Genetic Vulnerabilities

(A) Schematic of discovery platform for target/biomarker relationships.

(B) Genome-wide view of relative genomic DNA content, mRNA content, and RNAi toxicity in HCC4017 by two independent siRNA libraries (orange indicates Z < −3).

(C) Penetrance of the HCC4017 RNAi hits in 22 NSCLC lines.

(D) Gene ontology (%) of the private (n = 30; response in 1–2 lines) and public (n = 48; response in > 2 lines) RNAi hits. Subgraphs from the PPI network (see Figure S1H) are displayed in the boxes.

See also Figure S1, Tables S1, S2, and S3, and Data S1, S2, S4, S5, and S6.

to nontumorigenic bronchial epithelial cells (Data S5; Figure S1C). Cell lines from the two tails of the toxicity profile, derived from testing *CFLAR* depletion in 22 NSCLC lines, were selected for interrogation of molecular features correlating with sensitivity to *CFLAR* depletion (Figure 2A). From whole-genome mRNA expression profiles, *PYCARD*, *IFIT2*, and *IFIT3* were identified as the top-ranked genes commonly upregulated in *CFLAR*-dependent versus *CFLAR*-independent cell lines (Figure 2A, bottom panel). This expression model was sufficient to predict additional *CFLAR*-dependent cell lines from an unsupervised hierarchical cluster of a panel of 34 lines outside the original discovery set (Figure S2A). FLIP restrains execution of programmed cell death pathways through direct suppression of caspase-8 (Tschopp et al., 1998). FLIP addiction, therefore, infers the presence of latent death signals that are released upon removal of prosurvival restraints. This scenario is akin to the selective sensitivity of cancer cells to chemical mimics of SMAC (second mitochondria-derived activator of caspase) in the presence of tumor necrosis factor (TNF)-dependent apoptotic signaling, which is the consequence of uncoupling inhibitor of apoptosis proteins (IAPs) from otherwise active caspases (Tenev et al., 2011). However, only two of seven FLIP-dependent cell lines examined were

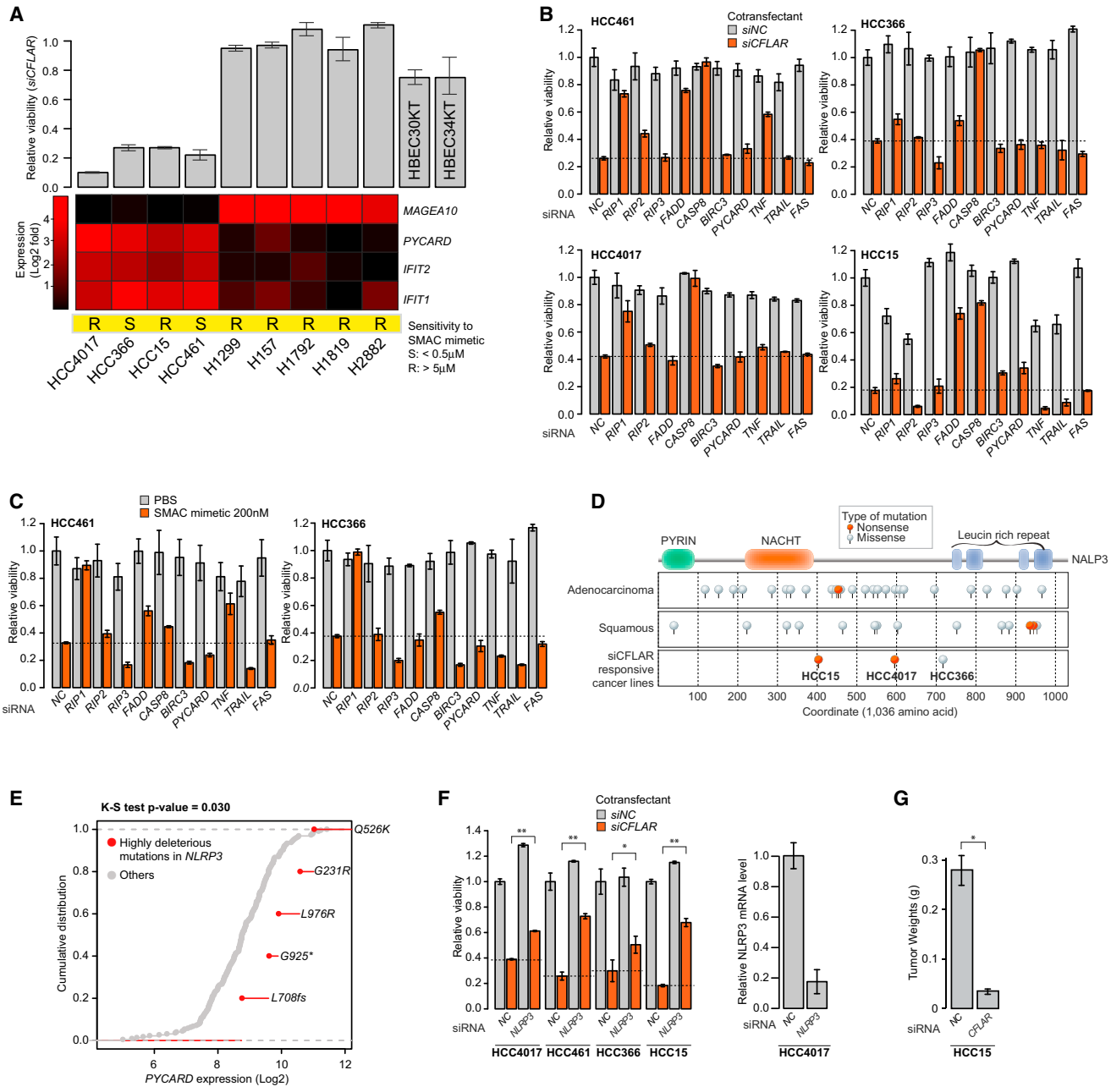

Figure 2. Context-Selective FLIP Addiction

(A) Bar plots indicate toxicity of *CFLAR* depletion in the most sensitive (relative viability < 0.3) and most resistant NSCLC cell lines (> 0.9) and two nontumorigenic lines. Heatmap indicates the gene-expression signature with the maximal bimodal distribution between groups. SMAC mimetic responsiveness is indicated as determined by LD50 (Table S5). Error bars indicate ± standard deviation (SD, n = 3).

(B) The indicated siRNAs were tested for consequences on *siCFLAR*-dependent toxicity within each of the *CFLAR*-dependent cell lines. Error bars as in (A).

(C) The indicated siRNAs were tested for consequences on SMAC mimetic-induced toxicity within each of the SMAC mimetic-responsive cell lines. Error bars as in (A).

(D) Pfam-A domain structure of NALP3 and maps of somatic mutations found.

(E) Empirical CDF plot of *PYCARD* expression from lung adenocarcinomas with or without highly deleterious mutations in *NLRP3* (TCGA).

(F) Consequence of NLRP3 depletion on CFLAR dependency; **p < 0.01, *p < 0.05 by two-sided unpaired Student's t test. siRNA-mediated *NLRP3* gene depletion is indicated as measured by quantitative PCR (qPCR) (right). Error bars as in (A).

(G) Tumor weights (g) following treatment with either control or CFLAR siRNAs. Error bars indicate ± standard error of the mean (SEM). *p = 0.026 by Wilcoxon rank sum test.

See also Figure S2 and Table S4.

additionally sensitive to SMAC-mimetic exposure, suggesting that FLIP can restrain programmed cell-death signals independently of SMAC-responsive IAPs (Figure 2A; Table S4). FLIP dependence did not correlate with expression of FLIP, its pro-death partner caspase-8, or SMAC-mimetic-resistant IAP2 (Petersen et al., 2010) (Figure S2B). However, sensitivity to FLIP depletion was completely reversed upon caspase-8 codepletion (Figure 2B). In contrast, SMAC-mimetic sensitivity was minimally affected by caspase-8 depletion and completely reversed by depletion of RIP1 kinase, an initiator of ripoptosome assembly that is negatively regulated by IAPs (Feoktistova et al., 2011; Tenev et al., 2011) (Figure 2C). Rescue of FLIP addiction by depletion of individual core components of the ripoptosome, or other canonical-death-pathway activators implicated in cancer, was cell line selective (Figure 2B). This suggests multiple distinct regulatory contexts within the NSCLC panel converge on FLIP-dependent restraint of caspase-8-initiated cell death. By its nature, the *PYCARD*, *IFIT1*, *IFIT2* expression signature is serving as a common indicator of these distinct contexts (Figure 2A). *IFIT1* and *2* are primary response genes induced by interferon and may ordinarily mediate cytotoxic responses to pathogen detection (Wathelet et al., 1988). *PYCARD* encodes ASC, a component of the inflammasome whose expression is also responsive to inflammasome activation signals (Masumoto et al., 2006; Strowig et al., 2012). Of note, HCC4017 harbors a somatic nonsense mutation in the inflammasome component *NLRP3* located in the linker region between the N-terminal NACHT domain and C-terminal leucine-rich repeat (LRR) domain (p.Y591*, Figure 2D). This alteration is predicted to encode a truncated, constitutively active protein, due to loss of LRR-domain-mediated repression of the NACHT domain (Hu et al., 2013). Derepression of NACHT domains promotes promiscuous NALP oligomerization and interaction with CARD domain proteins like ASC (Strowig et al., 2012). Somatic exonic *NLRP3* mutations are present in 16% of lung adenocarcinomas (Figure S2C, 21/129 in the LUAD TCGA samples) (Cerami et al., 2012), and *NLRP3* mutant adenocarcinomas were significantly enriched for NF-κB activity (Figure S2D), suggesting that *NLRP3* mutations in this context may be gain-of-function alterations. In support of this, highly deleterious mutations in *NLRP3* are significantly associated with *PYCARD* overexpression within the TCGA adenocarcinoma data set (Figure 2E), and there is an overall significant positive correlation between *PYCARD* and *NLRP3* expression (Figure S2E). Targeted sequencing revealed an analogous nonsense mutation in the FLIP-dependent cell line HCC15 (p.E401*) and a missense mutation in the FLIP-dependent cell line HCC366 (p.S727Y) (Barretina et al., 2012). Importantly, like caspase-8, codepletion of *NLRP3* relieved sensitivity of NSCLC lines to FLIP depletion, suggesting that NLRP3 activity helps drive FLIP addiction (Figure 2F). Furthermore, *NLRP3* mutation status was significantly associated with sensitivity to FLIP depletion (Figure S2F), and two additional *NLRP3* mutant NSCLC lines, identified from outside of the original tested panel, were also FLIP dependent (Figure S2G).

To model conservation of FLIP addiction within a tumorigenic context, we assessed the effects of *CFLAR* knockdown in a mouse xenograft model. Two weeks following subcutaneous injection of HCC15 cells, mice were randomly divided and treated with siRNAs incorporated into DOPC nanoliposomes (intraperitoneal [i.p.] administration) according to the following treatment groups (n = 10/group): control siRNA/DOPC and *CFLAR* siRNA/DOPC for 4 weeks. In comparison to the control siRNA group, tumors from the *CFLAR* siRNA group had a 87.2% reduction in tumor mass (p = 0.026; Figure 2G). These cumulative observations indicate that FLIP may represent an intervention opportunity in lung cancer linked to enrollment biomarkers that include *NLRP3* mutation status.

KRAS/LKB1 Mutation Status Specifies Coatomer 1 Addiction

Next, the mutation statuses for five recurrently mutated genes (*TP53*, *CDKN2A*, *KRAS*, *STK11* [*LKB1*], *NRAS*), collected by targeted sequencing, were queried for association with each of 85 siRNA toxicity profiles (Table S1; Data S5). Of note, co-occurrence of *KRAS*/*LKB1* mutations was significantly associated with sensitivity to depletion of COPI subunits ARCN1, COPB1, and COPA (Figure S3A). Approximately 6% of lung adenocarcinoma patients have co-occurring *KRAS*/*LKB1* mutations (Imielinski et al., 2012). COPI participates in retrograde transport, is required for endosome maturation (Huotari and Helenius, 2011; Razi et al., 2009), and is a CDC42 effector required for CDC42 transformation (Wu et al., 2000). From the intersection of the first-degree interaction network of HCC4017-essential genes (Figure S1H) and the commonality of responsiveness with the larger NSCLC cell-line panel (Figures 1C and 1D), we identified a total of five of seven components of the COPI. NSCLC cell lines representing the two tails of the distribution of sensitivity to COPI subunit depletion are shown in Figure 3A. Inhibition of COPI expression in multiple telomerase-immortalized bronchial epithelial cells was relatively innocuous and comparable to the consequence of COPI depletion in the COPI-resistant cancer lines (Figures 3A and 3B). Sensitivity to COPI depletion was recapitulated in soft-agar colony formation assays (Figure 3C). To assess the therapeutic utility of targeting the COPI subunit ARCN1, we utilized an orthotopic lung adenocarcinoma model capable of spontaneous metastasis. One week after surgical introduction of A549 cells into the left lung, mice were randomly divided and treated with siRNAs incorporated into DOPC nanoliposomes (i.p. administration) according to the following treatment groups (n = 10/group): control siRNA or *ARCN1* siRNA for 5 weeks. Treatment with *ARCN1* siRNAs led to substantial reductions in primary tumor size (92.9% by volume, p = 0.0087; 51.3% by left lung mass, p = 0.0032) as well as metastastic burden (90.4% reduction, p = 0.0015) (Figures 3D and S3B). This sensitivity correlated with hypophosphorylation of Rb and induction of cell-cycle arrest and apoptosis in vitro (Figures S3C and S3D). HCC4017 was an outlier with respect to LKB1 mutation status; however, this line has a defective AMPK response and therefore is the functional equivalent of COPI-addicted cell lines with compound lesions in *KRAS* and *LKB1* (Figure 3E). Importantly, co-occurrence of *KRAS* and *LKB1* mutations was a robust predictor of COPI addiction when tested in NSCLC cell lines outside the original discovery panel (Figure 3F), and LKB1 depletion was sufficient to sensitize *KRAS* mutant/*LKB1* wild-type cell lines to COPI depletion (Figure 3G).

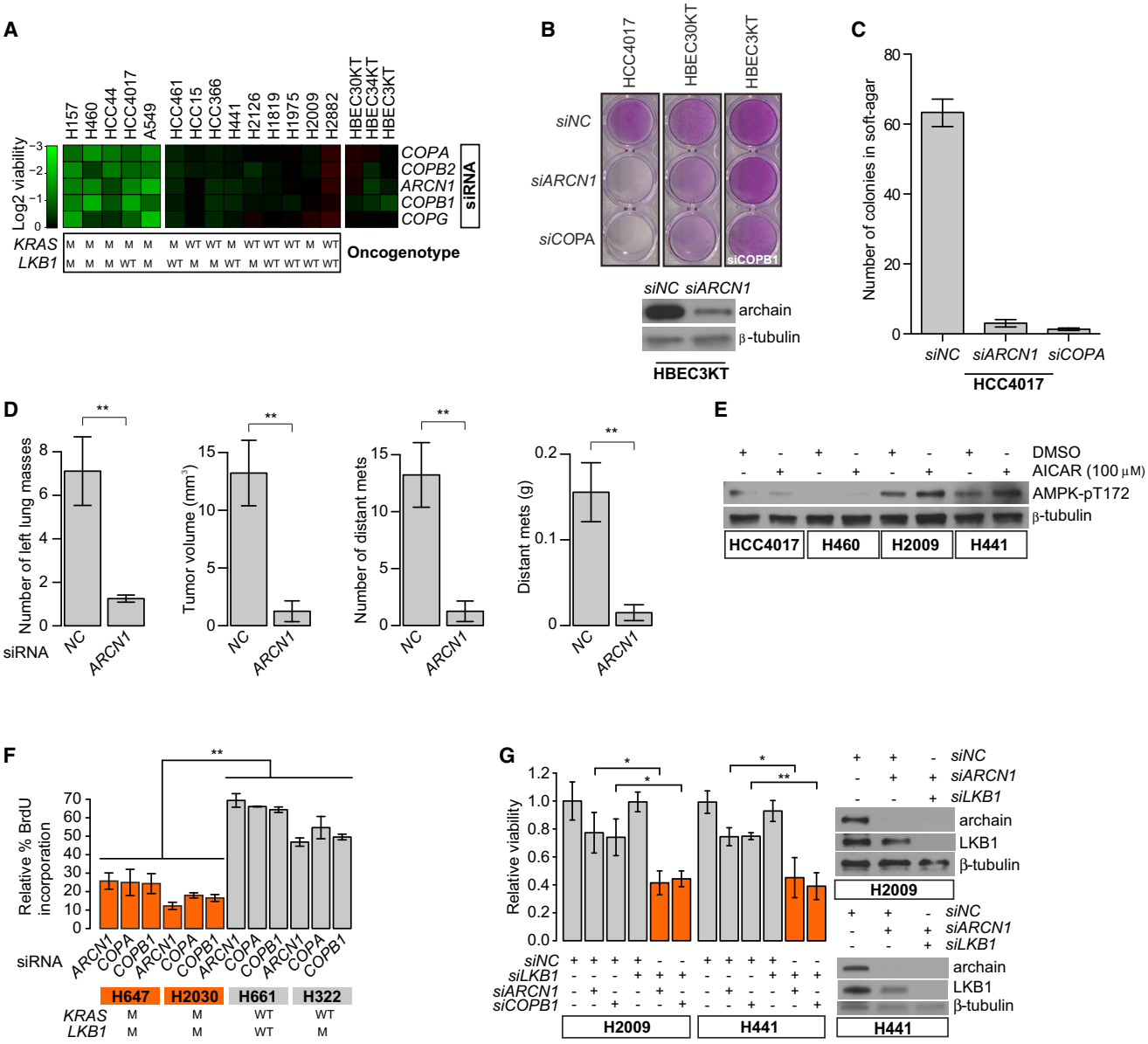

Figure 3. *KRAS*^{mut}/*LKB1*^{mut} Mutation Status Specifies Coatomer 1 Addiction

(A) RNAi toxicity profiles of the most sensitive and most resistant NSCLC lines to siRNA pools targeting COPI are shown. Mutation statuses of the *KRAS* and *LKB1* are indicated: M (mutant) or WT (wild-type).

(B) The indicated cell lines were transfected with the indicated siRNAs in 96-well plates and incubated for 48 hr followed by transfer to 24-well plates and incubation for an additional 6 days. Crystal violet-stained wells are shown. The immunoblot indicates persistence of target depletion in HBEC3 at the 8 day time point.

(C) The consequence of COPI depletion on HCC4017 colony formation in soft agar is shown. Error bars indicate ± SD, n = 3.

(D) Therapeutic effects of *ARCN1* siRNA in an orthotopic lung adenocarcinoma model (A549). Mets: metastasis. Error bars indicate ± SEM. One-sided Wilcoxon rank sum test p values were all < 0.01 (**).

(E) Consequence of AICAR on *AMPK* activation in two COPI-dependent (HCC4017 and H460) and two independent (H2009 and H441) *KRAS* mutant lines.

(F) Additional NSCLC lines from outside the test panel, with known *KRAS*^{mut}/*LKB1*^{mut} status, were assayed for BrdU incorporation to detect consequences of COPI depletion on proliferation as shown. Error bars as in (C).

(G) Consequence of *LKB1*/COPI codepletion in *KRAS* mutant cells. Immunoblots indicate target depletion. Error bars as in (C).

See also Figure S3.

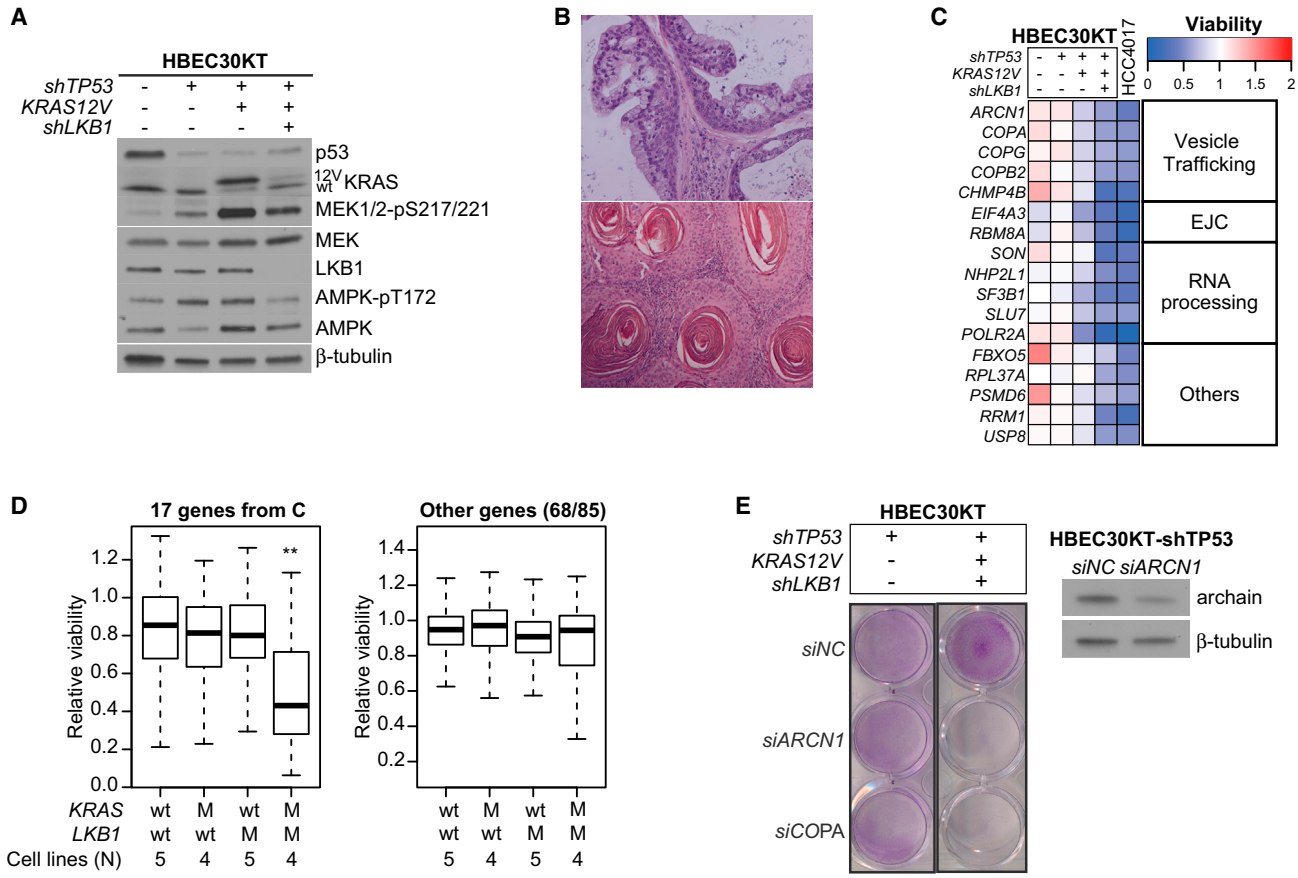

Figure 4. Oncogenic *KRAS* together with *LKB1* Loss Is Sufficient to Induce COPI Addiction

(A) Steady-state accumulation of the indicated proteins and phospho-proteins was assessed by immunoblot of whole-cell lysates from the indicated HBEC30KT derivatives.

(B) Representative hematoxylin and eosin staining (H&E) images of xenograft tumors formed upon subcutaneous inoculation of HBEC30KT-*shTP53*/*KRAS*^{G12V}/*shLKB1*, indicating mixed adenosquamous (top) and squamous (bottom) histology.

(C) Toxicity profile of the HCC4017 siRNA hits within the HBEC30KT progression series. The 17/85 siRNAs selectively toxic to the *KRAS*^{mut}/*LKB1*^{mut} cell lines are shown.

(D) Viability distributions of siRNA pools from 4C across 18 NSCLC lines with the indicated genotypes. Box plot whiskers extend to ± 1.5 interquartile range (IQR). Two-sided K-S test p values for all pair comparisons against the double mutants are less than 10^{-10} (**).

(E) The indicated cells were stained with crystal violet as in Figure 3B. Immunoblot indicates persistence of target depletion in resistant cells at the 8 day time point.

See also Figure S4.

Oncogenic *KRAS* together with *LKB1* Loss Is Sufficient to Induce COPI Addiction

To evaluate the sufficiency of compound *KRAS* and *LKB1* perturbation for induction of COPI addiction, we engineered a series of HBEC30KT derivatives with stepwise stable suppression of p53, stable expression of *KRAS*^{G12V}, and stable suppression of *LKB1* (Figures 4A, S4A, and S4B). Among these, only the final derivative was tumorigenic in immune-compromised mice, and tumors presented with mixed adeno/squamous characteristics (Figure 4B). This mixed morphology is strikingly similar to that observed in spontaneous mouse lung tumors that arise as a consequence of *Kras*^{G12V} expression in an *Lkb1* null background (Ji et al., 2007). A screen of 85 siRNA pools corresponding to the HCC4017-essential genes, within the HBEC30KT isogenic progression series, revealed acquired vulnerability to 17 targets within the *KRAS*^{mut}/*LKB1*^{mut} background (Figure 4C). Sensitivity to depletion of these same 17 genes was significantly enriched in *KRAS*^{mut}/*LKB1*^{mut} NSCLC cell lines as compared to that in other NSCLC lines tested (Figure 4D). COPI subunits were present in this context, indicating that *KRAS*^{mut}/*LKB1*^{mut} status is sufficient to specify COPI addiction (Figure 4E).

The *KRAS*^{mut}/*LKB1*^{mut} NSCLC Subtype Mirrors the Mesenchymal (Claudin-Low) Subtype of Triple-Negative Breast Cancer

Gene set enrichment analysis (GSEA) of whole-genome transcript profiles from COPI-sensitive versus COPI-resistant cell lines returned EMT, NF-κB, and tryptophan metabolism as significantly associated with *KRAS*^{mut}/*LKB1*^{mut} status (Table S5; Figure S5A; nominal $p < 0.01$), though none of these

signatures cleanly segregated the two classes. An siCOPI toxicity-associated gene-expression signature, with bimodal distribution, returned a more focused separation centered on chemokines and cytokines (Figure S5B, FDR < 0.001) reminiscent of the oncogenic RAS-induced secretory senescence phenotype (Coppé et al., 2008). Remarkably, 30% of the top 100 most differentially expressed genes, as defined by signal-to-noise ratio, intersected the molecular classification signature for the mesenchymal, or "claudin-low," subtype of triple-negative breast cancer (Prat et al., 2010) (Figure 5A, hypergeometric $p < 6.7 \times 10^{-16}$). Consistent with this, we found that three "claudin-low" breast cancer cell lines (Prat et al., 2010) were sensitive to COPI depletion as compared to cell lines corresponding to the lumenal A or basal A subtypes (Figure 5B). The mesenchymal subtype of triple-negative breast cancer is an aggressive metastatic disease enriched with self-renewing tumor-initiating cells (Prat et al., 2010). Dichotomization of 272 molecularly and clinically annotated lung tumor samples, using the expression signature defined by COPI addiction, revealed significantly reduced overall survival and disease-free survival for patients harboring signature-positive tumors (Figures 5C and S5C). Importantly, this relationship was reproducible with an independent patient cohort and data set (Figure S5D).

To parse molecular correlates that may provoke COPI addiction, we employed a focused suppressor screen that queried genes and pathways enriched in the COPI-sensitive cell lines (Figures S5E and S5F; see Experimental Procedures for rationale). The most significant interaction recovered was interleukin-6 (IL-6) pathway activation (Figure S5E). IL-6 secretion was significantly elevated in the COPI-sensitive lung and breast cancer cell lines, including the HBEC30KT progression series (Figures S5G, S5H, and S5I). Oncogenic RAS expression was sufficient to induce IL-6 production; however, co-occurring loss of *LKB1* signaling enhanced this phenotype in human epithelial cells and in mouse tumors (Figures S5I, S5J, and S5K). Inhibition of IL-6 signaling by IL-6 depletion, IL-6R depletion, or Let-7 expression significantly suppressed COPI addiction (Figures 5D, 5E, 5F, and S5L).

IL-6 has been characterized as a RAS-responsive cytokine that promotes tumorigenesis in a paracrine fashion by provoking stromal remodeling of the tumor microenvironment (Coppé et al., 2008). Consistent with this, we found that IL-6 secretion was KRAS dependent in COPI-addicted cell lines (Figure 5G). Furthermore, the tryptophan metabolism expression signature associated with COPI-addicted ($KRAS^{mut}/LKB1^{mut}$) cell lines (Figure S5A) implicated aryl hydrocarbon receptor (AhR) signaling as a mechanism that may contribute to IL-6 production. AhR induces IL-6 production in metastatic glioma, and both kynurenine and kynurenic acid, produced during tryptophan synthesis, serve as endogenous AhR ligands (Opitz et al., 2011). Consistent with this, depletion of AhR or the AhR nuclear translocator (*ARNTL*) significantly reduced IL-6 secretion (Figure 5H). Taken together, these observations suggest that selection for IL-6 secretion within the tumor microenvironment has collateral consequences on tumor cell biology that provoke addiction to COPI function. COPI activity thus becomes a collateral vulnerability that, if targetable, may represent a precision intervention opportunity.

Lysosomal Maturation Is Required to Support Mitochondrial Oxidative Phosphorylation and Survival of $KRAS^{mut}/LKB1^{mut}$ NSCLC Cells In Vitro and In Vivo

LKB1/AMPK-dependent repression of acetyl-CoA carboxylases (ACC1/2) can deflect catastrophic accumulation of oncogenic *RAS*-induced reactive oxygen species in cultured cells. This is thought to occur by limiting consumption of NADPH by ACC for fatty-acid synthesis, which in turn increases the NADPH/$NADP^+$ ratio needed to maintain the cellular redox state (Jeon et al., 2012; Son et al., 2013). This presents a compelling mechanistic scenario whereby $KRAS^{mut}/LKB1^{mut}$ cells are selectively sensitized to perturbations that impair reduction of reactive oxygen. In contradiction to this expectation, we found that glutathione or N-acetyl cysteine failed to rescue COPI addiction and were instead individually toxic (Figure S5F). Furthermore, the free radical scavenger NDGA displayed synthetic toxicity to $KRAS^{mut}/LKB1^{mut}$ expression in the HBEC30KT background, consistent with the reported prosurvival role of reactive oxygen within the context of oncogenic *RAS* expression (Figure S6A) (Irani et al., 1997).

To help uncover the mechanistic basis of COPI addiction, we assembled a panel of chemical probes that (1) intersect biological processes coupled to COPI function, (2) inhibit signaling pathways dysregulated in the $KRAS^{mut}/LKB1^{mut}$ background, or (3) engage cell-stress responses predicted to be induced by COPI depletion. The dose-dependent toxicity response to these compounds was then measured across 20 cell lines. Within this panel, the vacuolar ATPase inhibitor bafilomycin A1 (bafA) was discovered to have significant selective toxicity against the $KRAS^{mut}/LKB1^{mut}$ cell lines (Figure 6A) independent of ROS (Figures S6B and S6C). Like COPI depletion, exposure to 50 nM bafA for 48 hr induced CDKI accumulation, Rb hypophosphorylation, and caspase activation (Figure S6D). This suggests that $KRAS^{mut}/LKB1^{mut}$ cells may be selectively dependent upon lysosomal maturation, which is itself dependent upon COPI complex activity (Huotari and Helenius, 2011; Razi et al., 2009). A comparison of steady-state organelle accumulation revealed dramatic enrichment of acidic lysosomes in $KRAS^{mut}/LKB1^{mut}$ cells as compared to COPI-insensitive cells (Figure S6E). Furthermore, gain of COPI dependency through LKB1 depletion in a KRAS mutant NSCLC line, H2009, was coupled to the accumulation of the lysosomal membrane protein LAMP2 (Figure S6F). The elevated lysosomal activity in $KRAS^{mut}/LKB1^{mut}$ cells was reversed upon COPI subunit depletion independently of detectable morphological perturbation of the Golgi (Figures 6B and S6G) and by bafA concentrations below those required to inhibit lysosomal acidification of non-$KRAS^{mut}/LKB1^{mut}$ NSCLC cells (Figure S6H). A gene-expression feature (top-ranked GO term by GSEA) associated with COPI dependency and $KRAS^{mut}/LKB1^{mut}$ status was the enrichment of energy derivation by oxidation (Table S5; Figure S6I). Related to this, we noted that COPI depletion, exposure to bafA, or exposure to a structurally distinct vATPase inhibitor, saliphenylhalamide A (saliPhe) (Lebreton et al., 2008), resulted in the concomitant appearance of dysmorphic mitochondria in $KRAS^{mut}/LKB1^{mut}$ cells (Figures 6B and 6C) but not in bafA-resistant cells (Figure S6J). This altered morphology corresponded to reduced oxygen-consumption rates together with increased extracellular

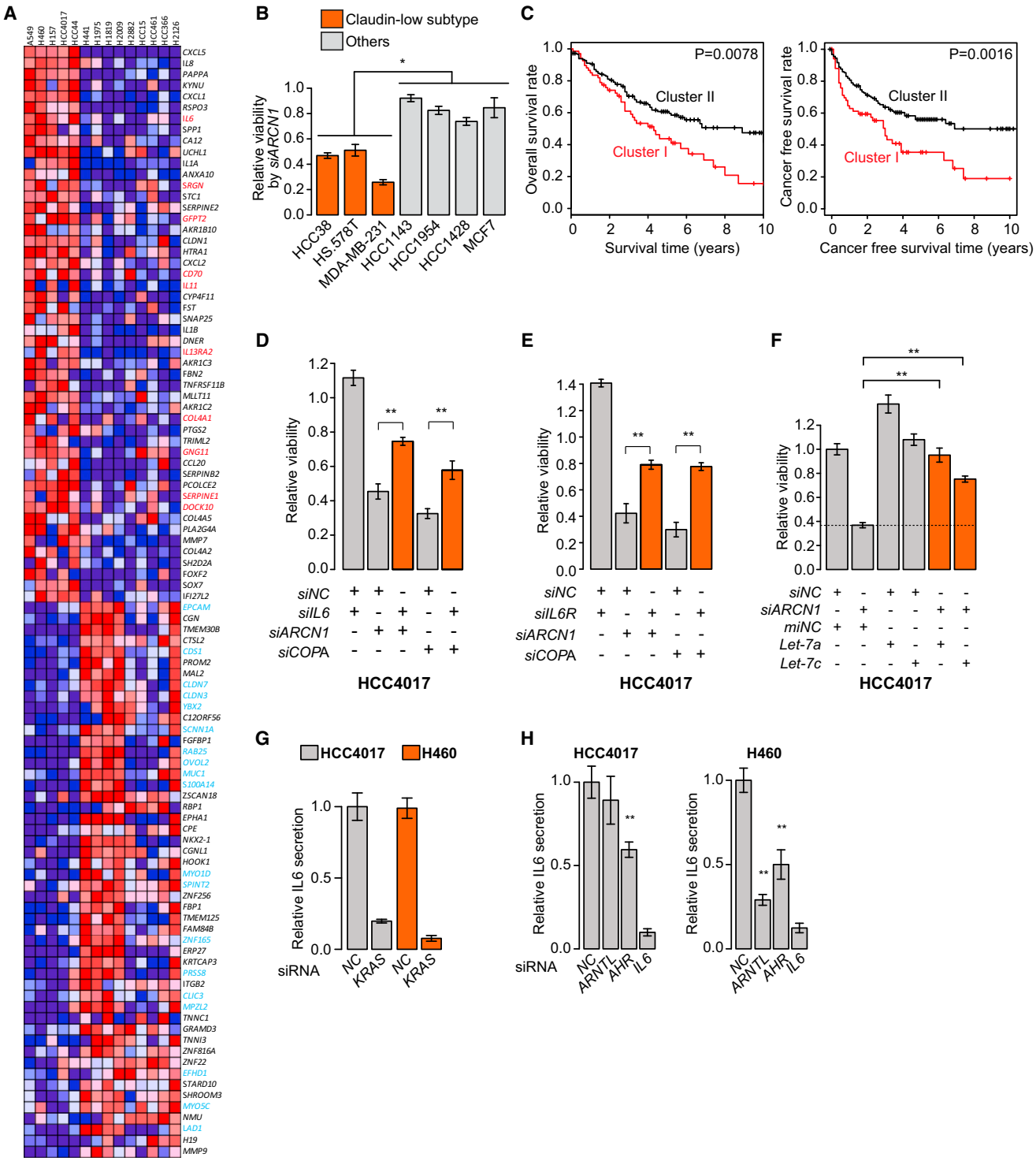

Figure 5. The *KRAS*^{mut}/*LKB1*^{mut} NSCLC Subtype Mirrors the Mesenchymal (Claudin-Low) Subtype of Triple-Negative Breast Cancer

(A) Top 100 differentially regulated genes as identified by signal-to-noise ratio between COPI-dependent and -independent cancer lines. Claudin-low signature genes are indicated in red for upregulated (10/437) and blue (19/370) for downregulated genes, hypergeometric $p < 6.7 \times 10^{-16}$.

(B) Selective consequence of *ARCN1* depletion on the viability of breast cancer cell lines. Error bars indicate ± SD, n = 3.

(C) Patient cohorts with the COPI-addicted gene-expression signature (Cluster I) show poor prognosis. Kaplan-Meier plots are shown for overall (left) and cancer-free survival (right) of the patient populations dichotomized as described in Figure S5C. p values are log-rank test.

(legend continued on next page)

acidification rates, suggesting impaired oxidative phosphorylation and concomitant induction of glycolysis (Figures 6D and S6K). However, this mitochondrial dysfunction was not coupled to loss of mitochondrial membrane potential (Figure S6L). Rather, bafA and saliPhe inhibited incorporation of heavy carbons from ^{13}C-labeled glucose or glutamine into citrate, consistent with inhibition of the mitochondrial TCA cycle (Figure 6E).

Perhaps through a futile adaptive response, loss of TCA-cycle activity was paralleled by increased glucose and glutamine consumption concomitant with conversion to secreted lactate and glutamate (Figures S6M and S6N). This phenotype was also observed in response to COPI depletion (Figure S6O). Finally, we found that direct inhibition of vATPase assembly by ATP6V1B2 depletion was sufficient to prevent lysosomal acidification (Figure 6F) and inhibit mitochondrial respiration (Figure 6G). These observations indicate that lysosomal maturation is selectively required to support mitochondrial function in *KRAS^{mut}/LKB1^{mut}* cells. The coupling of this vulnerability to a genetic background that promotes energetic stress led us to consider the possibility that *KRAS^{mut}/LKB1^{mut}* cells are selectively dependent upon hydrolysis of lysosomal macromolecules for supply of mitochondrial TCA-cycle substrates. We found that delivery of cell-permeable pyruvate (methyl pyruvate, MP) or α-ketoglutarate (dimethyl-2-oxoglutarate, MOG), two major carbon sources fueling the mitochondrial TCA cycle, rescued cell viability and mitochondrial respiration in the presence of bafA (Figures 6H and S6P). Importantly, this rescue occurred without restoration of lysosomal acidification (Figure S6Q), consistent with the hypothesis that lysosomes support mitochondrial function through supply of an obligate nutrient source in *KRAS^{mut}/LKB1^{mut}* cells. Perdurant acetyl-CoA carboxylase activity in the *KRAS^{mut}/LKB1^{mut}* background is likely a mechanism that helps drive lysosomal addiction, as ACC1 depletion rescued cell viability in the presence of bafA (Figure 6I). We suspect that ACC1 inactivation is facilitating productive fatty-acid beta-oxidation as an alternate energy source due to depletion of malonyl-coA, an ACC1 product that inhibits mitochondrial import of long-chain fatty acids (Abu-Elheiga et al., 2001). These observations present a compelling argument for consideration of lysosomes as a metabolic bottleneck by which to target energy homeostasis in *KRAS^{mut}/LKB1^{mut}* lung cancer cells. To model this in vivo, mice bearing established HCC4017 subcutaneous xenografts were exposed to saliPhe (12.5 mg/kg/day, n = 5) or vehicle (n = 4) using osmotic pumps implanted i.p. The pumps eluted drugs for ~17 days, at which time tumors in the vehicle-treated group were 174% larger, whereas tumors in the saliPhe-treated animals were 40% of the starting volume. The effect of saliPhe was durable as tumors were allowed to grow for an additional 35 days in the absence of further drug exposure, and tumors in saliPhe-treated animals were 4-fold smaller than tumors in vehicle-treated animals (0.116 ± 0.27 g versus 0.46 ± 0.13 g; $p < 0.05$) (Figure 6J).

A Gene-Expression Model Predicts Sensitivity to a Synthetic Compound, Indolotriazine

To collect additional chemical probes for detection of subtype-selective vulnerabilities in NSCLC, we examined 352 compounds (out of 230,000 screened) that were selectively toxic to HCC4017 cells versus HBEC30KT at 2.5 μM (Figure S7A; Data S3-1 and S3-2). Two of the 352 compounds displayed bimodal LD50s across 12 NSCLC lines (>3-fold separation of "sensitive" versus "resistant" lines). Among these, an indolotriazine, SW044248, was selectively toxic in 18/74 NSCLC lines and innocuous up to the highest testable dose in four different telomerase-immortalized bronchial epithelial cell lines (Figure 7A; Data S3-3). To inform the mode of action, resistant HCC4017 subclones were isolated following long-term exposure to the compound. RNA-seq identified differential gene-expression responses to SW044248, in parental versus resistant HCC4017 variants, corresponding to a strong and selective ER stress-response signature (Figure 7B; Data S7) (Hetz, 2012). Consistent with this, CHOP and IRE1α were robustly induced within 24 hr of exposure to SW044248 (Figure 7C). This response was uniform among the SW044248-sensitive NSCLC lines but absent in resistant lines (Figure 7D). The latter is most likely a consequence of selective vulnerability rather than selective exposure as equivalent SW044248 accumulation and stability were observed in both sensitive and resistant cell lines as detected by gas chromatography-mass spectrometry (GC-MS) (Figures S7B and S7C).

To identify features that may predispose to the indolotriazine sensitivity, we searched for gene-expression networks that correlated with the compound responsiveness within the cell-line panel. Two ER stress-related networks were ranked among the top discoverable networks by edge flux (EF) and process flux (PF) values (Figure S7D) (Komurov et al., 2012). In addition, an elastic net regression model using basal gene-expression data identified seven genes (*C8G*, *PSG7*, *ACOT6*, *DEPDC5*, *MMP16*, *UBR1*, and *CYP4F22*) as robust indicators of indolotriazine responsiveness (Figures 7E and S7E). Feature performance was filtered by a 200× bootstrapping protocol, from which all features were detected at frequencies > 50%. The sum of the weighted features in this model were used to predict SW044248 sensitivity from a panel of 38 NSCLC lines outside of the training set. HCC2429 and H1770 represented the two tails (sensitive and resistant) of the distribution of predicted IC_{50}s, which were empirically validated with eight-point dose-response curves (Figure 7F). Twenty-three of 231 lung adenocarcinomas were within the left-hand tail of the frequency distribution of elastic net scores, suggesting that ~10% of tumors contain expression features consistent with SW044248 sensitivity (Figure S7F).

DISCUSSION

Widespread evidence indicates that acquired vulnerabilities, arising in the course of tumor evolution, represent key

(D–F) Consequences of codepletion of *IL6* (D) and *IL6R* (E) or exposure to *Let-7* family of miRNA mimics (F) on siRNA toxicity of indicated COPI subunits. Error bars as in (B).

(G and H) IL-6 secretion was measured by ELISA post-transfection of the indicated siRNAs in the indicated cell lines. Values were normalized to cell number. **$p < 0.01$, *$p < 0.05$, two-sided unpaired Student's t test; error bars as in (B).

See also Figure S5 and Table S5.

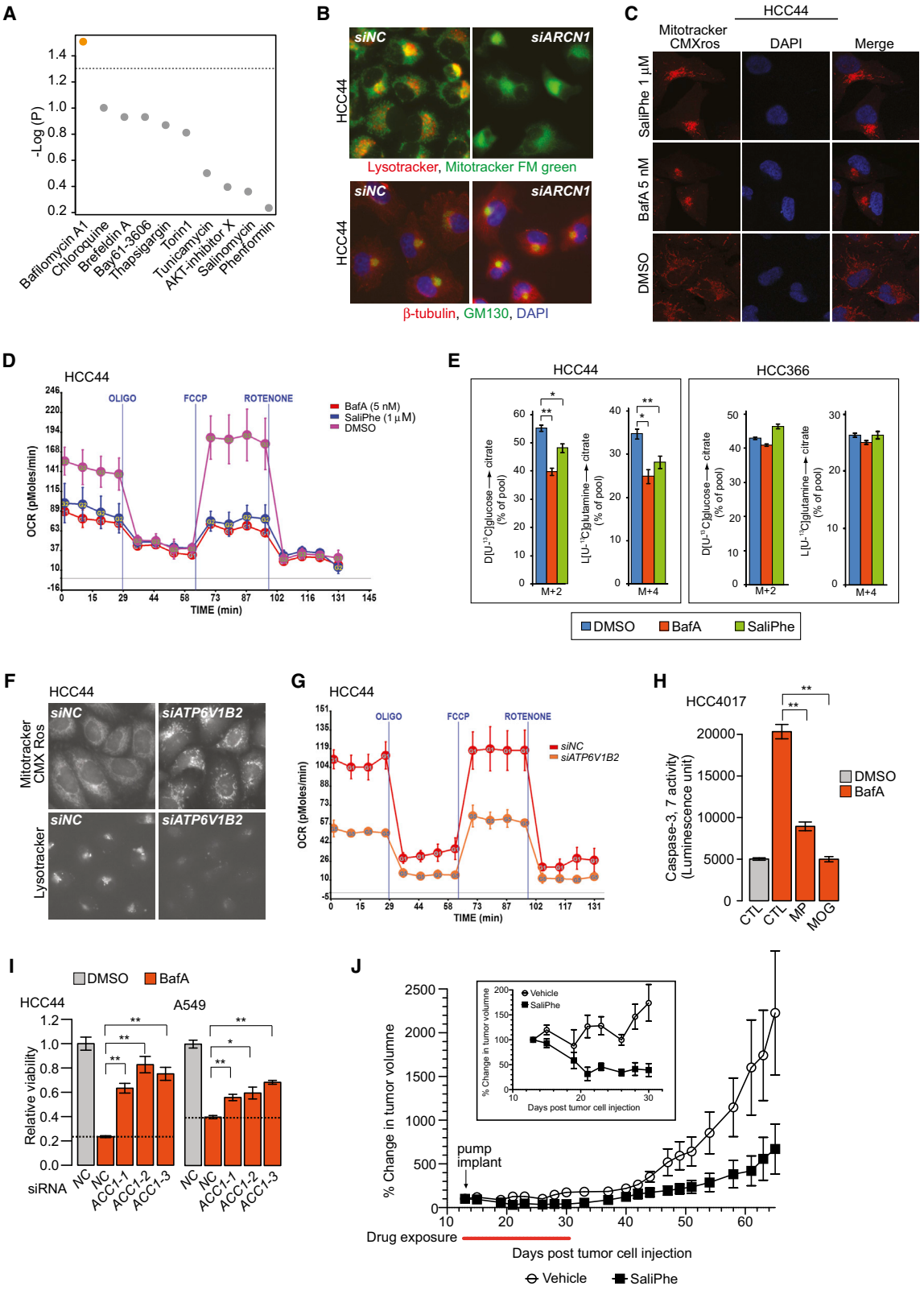

(legend on next page)

therapeutic intervention opportunities. Starting from within the context of a single lung adenocarcinoma patient, we identified genetic and chemical vulnerabilities selectively associated with tumorigenicity. However, the incidence of these vulnerabilities, within a lineage-restricted panel of NSCLC-derived cell lines, was highly idiosyncratic. By focusing on perturbations with significant activity in a large cell-line panel, we could begin to detect intervention targets linked to molecular subtypes that specify target sensitivity and have reasonable frequencies of representation within the lung cancer patient population.

A robust, but previously unrecognized, genotype/phenotype relationship uncovered by this approach is the selective addiction of *NLRP3* mutant cells to FLIP. FLIP is widely recognized as a candidate oncology target opportunity due to its role in deflection of caspase-8-dependent programmed cell death (Safa and Pollok, 2011), but distinct genetic settings that specify FLIP dependence had not been elaborated. NLRP3 triggers inflammasome assembly and consequent activation of NF-κB and cytokine production upon detection of microbial infection or cellular injury (Bryant and Fitzgerald, 2009; Manji et al., 2002). It is constitutively expressed in epithelial cells but, in the absence of "danger signals," is thought to exist in an autoinhibited state (Hu et al., 2013). Of note, mutations in NLRP3 result in persistent cytokine production and are the causal lesions for CAPS, a group of congenital autoinflammatory diseases (Hoffman et al., 2001). In light of *NLRP3*'s role in innate immune signaling, it is reasonable to suspect that the frequent *NLRP3* alterations found in lung tumors could contribute to tumor growth by inflammatory signal-mediated recruitment of stromal cell populations. In this scenario, positive selection for *NLRP3* variants that stimulate production of a protumorigenic niche creates a collateral dependence on FLIP inhibition of apoptosis. The mechanistic coupling may be direct given recent observations that the NLRP3 inflammasome can bind and activate caspase-8 (Gringhuis et al., 2012; Pierini et al., 2012; Sagulenko et al., 2013). Direct chemical inhibition of FLIP is not currently available; however, a variety of small molecules that inhibit FLIP expression or enhance FLIP degradation have been reported (Safa and Pollok, 2011; Zhao et al., 2011) and may represent a path forward for pharmacological targeting of NLRP3 mutant lung cancers.

Detection of oncogenic KRAS-linked vulnerabilities is a high-priority, but often confounding, pursuit in multiple neoplastic settings because of the frequency of representation of this oncogene in human tumors. Within the context of NSCLC cells, loss of LKB1 activity together with expression of oncogenic KRAS is required and sufficient to drive COPI addiction. This genetic interaction reinforces the notion that all KRAS cancers are not equivalent, and robust mapping of intervention opportunities must account for distinct collaborative alterations that result in distinct collateral vulnerabilities. COPI participates in a variety of dynamic membrane-trafficking events and is well studied for its role in support of retrograde transport (Lee et al., 2004). However, we found that the mechanistic basis of COPI addiction in the $KRAS^{mut}/LKB1^{mut}$ background is the obligate contribution of this protein complex to lysosome acidification. Chemical or genetic perturbation of lysosome maturation in $KRAS^{mut}/LKB1^{mut}$ cells resulted in mitochondrial malfunction and cell death. Mitochondrial dependence on lysosomal maturation was bypassed by supply of cell-permeable TCA-cycle substrates, including pyruvate and α-ketoglutarate. This, together with the observation that $KRAS^{mut}/LKB1^{mut}$ cells displayed signs of elevated lysosomal flux, strongly suggests that this molecular subtype requires consumption and hydrolysis of extracellular macromolecules for minimal supply of cellular metabolic intermediates. Recognition of lysosomal function as a context-dependent metabolic bottleneck is reinforced by three additional recent observations. First, the coupling of lysosome acidification capacity to mitochondrial health has been defined as a key determinant of cellular aging in yeast (Hughes and Gottschling, 2012). Second, pancreas cancer cells mount an adaptive response to glutamine starvation by induction of macropinocytosis and consequent consumption of extracellular macromolecules as an amino-acid supply route (Commisso et al., 2013). Third, dysregulation of mTORC1 drives addiction to

Figure 6. Lysosomal Maturation Is Required to Support Mitochondrial Oxidative Phosphorylation and Survival of $KRAS^{mut}/LKB1^{mut}$ NSCLC Cells In Vitro and In Vivo

(A) Compound mimic screen. The indicated compounds were tested over 11 doses (2× serial dilution) for toxicity in HCC4017 and $KRAS^{mut}/LKB1^{mut}$ lines (n = 6) versus HBEC30KT and others (n = 14). Area under the curve (AUC) was estimated by the sum of % viability over testing doses. One-sided two-sample K-S tests were performed to discriminate compounds with selective activity. K-S test p values in negative log scale were used to generate the plot.

(B) HCC44 cells, transfected with the indicated siRNAs were stained with the indicated dyes and antibodies. Seventy-one percent of *siARCN1* cells were Lysotracker negative versus 3.0% of *siNC* cells; p value < 2.2×10^{-16}; Fisher's exact test.

(C) Confocal imaging of mitochondrial morphology after 42 hr exposure to vATPase inhibitors. Ninety-two percent of bafA-treated and 85% saliPhe-treated cells had dysmorphic mitochondria versus 2.7% with DMSO; p value < 2.2×10^{-16} for both; Fisher's exact test.

(D) Oxygen consumption rates (OCR) of HCC44 cells exposed to the indicated compounds. Error bars indicate ± SD, n = 3.

(E) Mass isotopomer analysis of citrate in HCC44 cells cultured with D[U-^{13}C]glucose and unlabeled glutamine (left for each cell line) or L[U-^{13}C]glutamine and unlabeled glucose (right for each cell line) after exposure to 10 nM BafA or 1 μM saliPhe for 16 hr. **p < 0.01, *p < 0.05, two-sided t test, error bars as in (B).

(F) Live-cell images obtained as in (B) and (C).

(G) As in (D), except that HCC44 cells were transfected with the indicated siRNAs prior to the assay. Ninety-three percent of *siATP6V1B2* cells had dysmorphic mitochondria versus 0% of *siNC* cells; p value < 2.2×10^{-16}; Fisher's exact test; error bars as in (B).

(H) Caspase-3 and -7 activity was measured after exposure of HCC4017 to DMSO or bafA (5 nM) for 48 hr together with methyl pyruvate (8 mM), dimethyl-2-oxoglutarate (MOG, 5 mM), or water (CTL). Error bars as in (B).

(I) Indicated siRNAs were tested for consequences on bafA (10 nM) dependent toxicity in HCC44 and A549. Cells were exposed to bafA 48 hr post-transfection. Error bars as in (B).

(J) 2.5×10^6 HCC4017 cells were injected subcutaneously into NOD/SCID mice. Tumor volume versus days post-tumor injection is displayed for mice treated with saliPhe or saline as indicated.

Error bars indicate ± SEM. See also Figure S6 and Table S5.

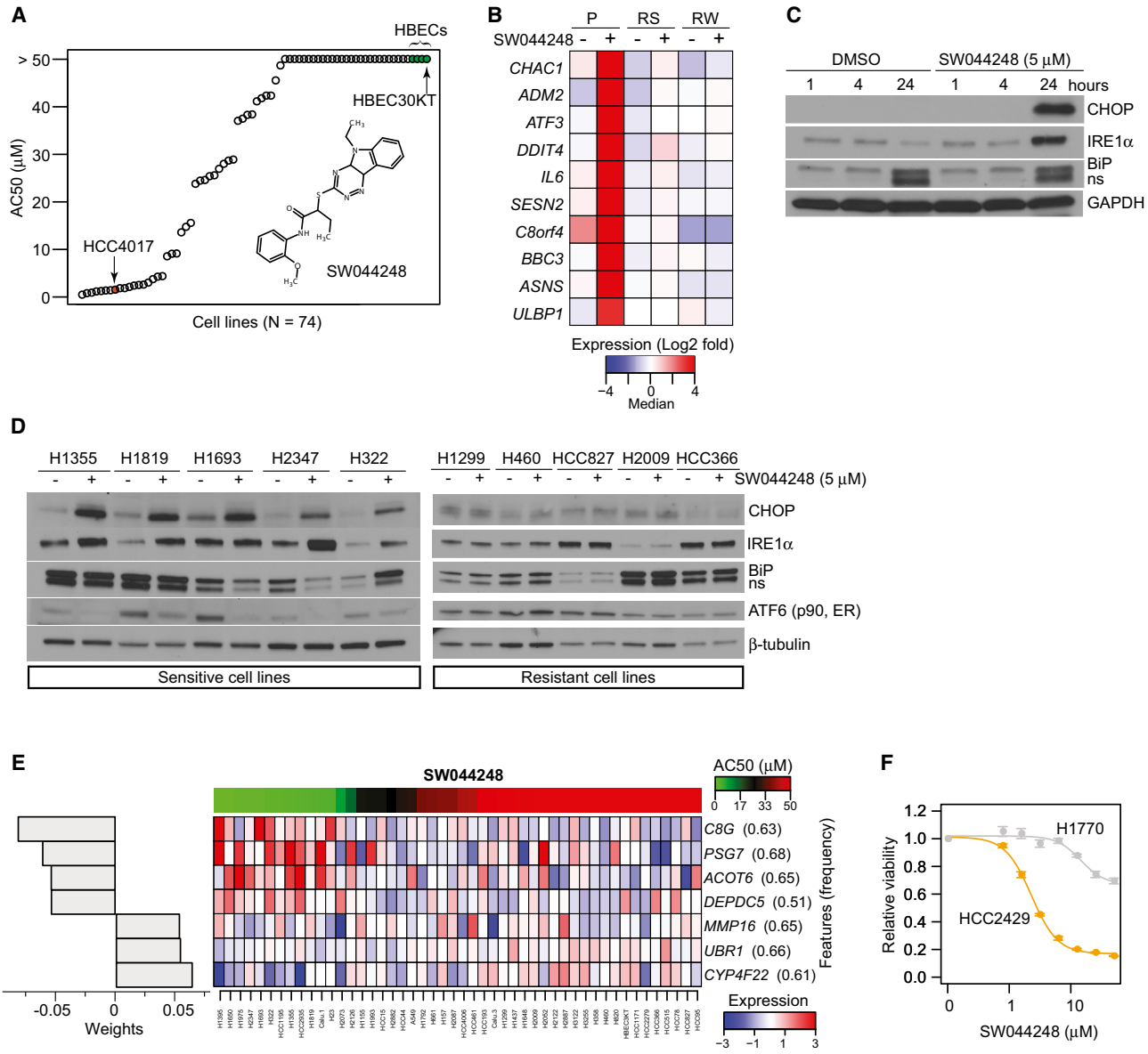

Figure 7. A Gene-Expression Model Predicts Sensitivity to an Indolotriazine

(A) AC50 for the HCC4017-selective synthetic indolotriazine derivative against 74 additional NSCLC cell lines and immortalized HBECs.

(B) Top 10 differential gene-expression responses to SW044248 (2 μM, 6 hr) in HCC4017 parental (P) and resistant clones (RS, RW) as detected by RNA-seq (ANOVA, $p < 0.005$, Data S7).

(C) Relative accumulation of CHOP, IRE1α, and BiP proteins upon exposure of HCC4017 for the indicated times.

(D) As in (C) except with a 24 hr exposure with indicated cell lines.

(E) Predictive basal gene-expression features for SW044248 sensitivity in 48 NSCLCs by elastic net regression modeling. Compound response (AC50) is indicated in the top row. Predictive gene-expression features (normalized by sample median) across 48 NSCLCs are shown. Bar plot on the left indicates the average weight for the corresponding feature as determined from a 200× bootstrapping analysis. Frequency of feature occurrence is shown in parenthesis.

(F) Dose-response curves for a predicted sensitive cell line, HCC2429, and a predicted resistant cell line, H1770, based on the expression signature-derived scoring function. Error bars indicate ± SD, n = 3.

See also Figure S7 and Data S3-1, S3-2, S3-3, and S7.

consumption of exogenous desaturated lipids to support endomembrane expansion (Young et al., 2013). The incidence of co-occurring *KRAS* and *LKB1* mutations in NSCLC is estimated to be 6% of all lung adenocarcinomas, which corresponds to 5,000 new cancer patients per year in the USA alone. Establishing $KRAS^{mut}/LKB1^{mut}$ mutation status as a robust indicator of COPI addiction presents the opportunity to exploit clinical laboratory-based detection of somatic alterations in these genes as an enrollment biomarker to stratify patient populations predicted to respond to chemical perturbation of lysosome maturation.

Screening of a large diversity-based collection of synthetic small molecules revealed a chemical liability in cancer cell lines that share distinct gene-expression features. Although the target of this compound remains to be defined, the mode-of-action appears to be through selective mobilization of the unfolded protein response and consequent cell death. Of interest, a relatively large but highly selective cohort is responsive to the indolotriazine SW044248 (24% of cell lines tested). Thus, SW044248 can be described as a chemical discriminator of a distinct NSCLC subtype. If indolotriazine sensitivity is preserved in the in vivo setting, this chemical discriminator becomes a lead for therapeutically relevant pharmacological characterization of discrete vulnerabilities within this subtype.

In summary, cell-based exploration of lung cancer intervention opportunities can be a rich source of target discovery given sufficient commonality of sensitivity and resolution of molecular correlates. Starting with disease-cell-selective vulnerabilities present in isolates from a single lung cancer patient, two distinct molecular targets were identified, linked to two distinct genetic lesions, which together are represented in over 25% of lung adenocarcinoma patients. In addition, a chemically defined vulnerability was identified that is associated with an expression-based biomarker estimated to occur in 10% of lung cancer patients.

EXPERIMENTAL PROCEDURES

Materials, procedures, and computational analysis including deep sequencing, high-throughput screening, and associated data processing and analysis; mouse xenograft studies, mitochondrial respiratory potential, metabolic flux, pharmacokinetic analysis, and elastic net regression modeling; and other statistical processing protocols are detailed in the Extended Experimental Procedures.

SUPPLEMENTAL INFORMATION

Supplemental Information includes Extended Experimental Procedures, seven figures, five tables, and seven data sets and can be found with this article online at http://dx.doi.org/10.1016/j.cell.2013.09.041.

ACKNOWLEDGMENTS

We thank John Heymach and Lauren Byers (MD Anderson) for sharing HCC4017-SNP array data; Robert Collins for sharing Exome-seq data from normal tissue samples; and Peter Hammerman for sharing TCGA gene expression data. This study was supported by grants from the NIH (CA71443, CA129451, CA176284, CA148225, and CA70907), the Robert Welch Foundation (I-1414), the Logenbaugh Foundation, and CPRIT (RP101496, RP110708). Shared facilities were supported in part by P30CA142543. M.A.W., M.G.R., B.A.P., and J.D.M. are members of the NCI Cancer Target and Discovery (CTD^2) Network.

Received: June 30, 2013
Revised: August 15, 2013
Accepted: August 30, 2013
Published: October 24, 2013

REFERENCES

Abu-Elheiga, L., Matzuk, M.M., Abo-Hashema, K.A., and Wakil, S.J. (2001). Continuous fatty acid oxidation and reduced fat storage in mice lacking acetyl-CoA carboxylase 2. Science *291*, 2613–2616.

Barretina, J., Caponigro, G., Stransky, N., Venkatesan, K., Margolin, A.A., Kim, S., Wilson, C.J., Lehár, J., Kryukov, G.V., Sonkin, D., et al. (2012). The Cancer Cell Line Encyclopedia enables predictive modelling of anticancer drug sensitivity. Nature *483*, 603–607.

Bryant, C., and Fitzgerald, K.A. (2009). Molecular mechanisms involved in inflammasome activation. Trends Cell Biol. *19*, 455–464.

Cancer Genome Atlas Research Network. (2012). Comprehensive genomic characterization of squamous cell lung cancers. Nature *489*, 519–525.

Cerami, E., Gao, J., Dogrusoz, U., Gross, B.E., Sumer, S.O., Aksoy, B.A., Jacobsen, A., Byrne, C.J., Heuer, M.L., Larsson, E., et al. (2012). The cBio cancer genomics portal: an open platform for exploring multidimensional cancer genomics data. Cancer Discov. *2*, 401–404.

Commisso, C., Davidson, S.M., Soydaner-Azeloglu, R.G., Parker, S.J., Kamphorst, J.J., Hackett, S., Grabocka, E., Nofal, M., Drebin, J.A., Thompson, C.B., et al. (2013). Macropinocytosis of protein is an amino acid supply route in Ras-transformed cells. Nature *497*, 633–637.

Coppé, J.P., Patil, C.K., Rodier, F., Sun, Y., Muñoz, D.P., Goldstein, J., Nelson, P.S., Desprez, P.Y., and Campisi, J. (2008). Senescence-associated secretory phenotypes reveal cell-nonautonomous functions of oncogenic RAS and the p53 tumor suppressor. PLoS Biol. *6*, 2853–2868.

Feoktistova, M., Geserick, P., Kellert, B., Dimitrova, D.P., Langlais, C., Hupe, M., Cain, K., MacFarlane, M., Häcker, G., and Leverkus, M. (2011). cIAPs block Ripoptosome formation, a RIP1/caspase-8 containing intracellular cell death complex differentially regulated by cFLIP isoforms. Mol. Cell *43*, 449–463.

Gazdar, A.F., Girard, L., Lockwood, W.W., Lam, W.L., and Minna, J.D. (2010). Lung cancer cell lines as tools for biomedical discovery and research. J. Natl. Cancer Inst. *102*, 1310–1321.

Gringhuis, S.I., Kaptein, T.M., Wevers, B.A., Theelen, B., van der Vlist, M., Boekhout, T., and Geijtenbeek, T.B. (2012). Dectin-1 is an extracellular pathogen sensor for the induction and processing of IL-1β via a noncanonical caspase-8 inflammasome. Nat. Immunol. *13*, 246–254.

Guédat, P., and Colland, F. (2007). Patented small molecule inhibitors in the ubiquitin proteasome system. BMC Biochem. *8*(*Suppl 1*), S14.

Hetz, C. (2012). The unfolded protein response: controlling cell fate decisions under ER stress and beyond. Nat. Rev. Mol. Cell Biol. *13*, 89–102.

Hoffman, H.M., Mueller, J.L., Broide, D.H., Wanderer, A.A., and Kolodner, R.D. (2001). Mutation of a new gene encoding a putative pyrin-like protein causes familial cold autoinflammatory syndrome and Muckle-Wells syndrome. Nat. Genet. *29*, 301–305.

Hu, Z., Yan, C., Liu, P., Huang, Z., Ma, R., Zhang, C., Wang, R., Zhang, Y., Martinon, F., Miao, D., et al. (2013). Crystal structure of NLRC4 reveals its autoinhibition mechanism. Science *341*, 172–175.

Hughes, A.L., and Gottschling, D.E. (2012). An early age increase in vacuolar pH limits mitochondrial function and lifespan in yeast. Nature *492*, 261–265.

Huotari, J., and Helenius, A. (2011). Endosome maturation. EMBO J. *30*, 3481–3500.

Imielinski, M., Berger, A.H., Hammerman, P.S., Hernandez, B., Pugh, T.J., Hodis, E., Cho, J., Suh, J., Capelletti, M., Sivachenko, A., et al. (2012). Mapping the hallmarks of lung adenocarcinoma with massively parallel sequencing. Cell *150*, 1107–1120.

Irani, K., Xia, Y., Zweier, J.L., Sollott, S.J., Der, C.J., Fearon, E.R., Sundaresan, M., Finkel, T., and Goldschmidt-Clermont, P.J. (1997). Mitogenic signaling mediated by oxidants in Ras-transformed fibroblasts. Science *275*, 1649–1652.

Irmler, M., Thome, M., Hahne, M., Schneider, P., Hofmann, K., Steiner, V., Bodmer, J.L., Schröter, M., Burns, K., Mattmann, C., et al. (1997). Inhibition of death receptor signals by cellular FLIP. Nature *388*, 190–195.

Jacob, L.S., Wu, X., Dodge, M.E., Fan, C.W., Kulak, O., Chen, B., Tang, W., Wang, B., Amatruda, J.F., and Lum, L. (2011). Genome-wide RNAi screen reveals disease-associated genes that are common to Hedgehog and Wnt signaling. Sci. Signal. *4*, ra4.

Jänne, P.A., Gray, N., and Settleman, J. (2009). Factors underlying sensitivity of cancers to small-molecule kinase inhibitors. Nat. Rev. Drug Discov. *8*, 709–723.

Jeon, S.M., Chandel, N.S., and Hay, N. (2012). AMPK regulates NADPH homeostasis to promote tumour cell survival during energy stress. Nature *485*, 661–665.

Ji, H., Ramsey, M.R., Hayes, D.N., Fan, C., McNamara, K., Kozlowski, P., Torrice, C., Wu, M.C., Shimamura, T., Perera, S.A., et al. (2007). LKB1 modulates lung cancer differentiation and metastasis. Nature *448*, 807–810.

Komurov, K., Dursun, S., Erdin, S., and Ram, P.T. (2012). NetWalker: a contextual network analysis tool for functional genomics. BMC Genomics *13*, 282.

Lebreton, S., Jaunbergs, J., Roth, M.G., Ferguson, D.A., and De Brabander, J.K. (2008). Evaluating the potential of vacuolar ATPase inhibitors as anticancer agents and multigram synthesis of the potent salicylihalamide analog saliphenylhalamide. Bioorg. Med. Chem. Lett. *18*, 5879–5883.

Lee, M.C., Miller, E.A., Goldberg, J., Orci, L., and Schekman, R. (2004). Bidirectional protein transport between the ER and Golgi. Annu. Rev. Cell Dev. Biol. *20*, 87–123.

Luo, J., Solimini, N.L., and Elledge, S.J. (2009). Principles of cancer therapy: oncogene and non-oncogene addiction. Cell *136*, 823–837.

Lynch, T.J., Bell, D.W., Sordella, R., Gurubhagavatula, S., Okimoto, R.A., Brannigan, B.W., Harris, P.L., Haserlat, S.M., Supko, J.G., Haluska, F.G., et al. (2004). Activating mutations in the epidermal growth factor receptor underlying responsiveness of non-small-cell lung cancer to gefitinib. N. Engl. J. Med. *350*, 2129–2139.

Manji, G.A., Wang, L., Geddes, B.J., Brown, M., Merriam, S., Al-Garawi, A., Mak, S., Lora, J.M., Briskin, M., Jurman, M., et al. (2002). PYPAF1, a PYRIN-containing Apaf1-like protein that assembles with ASC and regulates activation of NF-kappa B. J. Biol. Chem. *277*, 11570–11575.

Masumoto, J., Kobayashi, H., Nakamura, T., Kaneko, Y., Ota, H., Hasegawa, M., Kobayashi, Y., Suzuki, T., Matsuda, K., Sano, K., et al. (2006). Regulation of the ASC expression in response to LPS stimulation is related to IL-8 secretion in the human intestinal mucosa. Biochem. Biophys. Res. Commun. *346*, 968–973.

Muller, F.L., Colla, S., Aquilanti, E., Manzo, V.E., Genovese, G., Lee, J., Eisenson, D., Narurkar, R., Deng, P., Nezi, L., et al. (2012). Passenger deletions generate therapeutic vulnerabilities in cancer. Nature *488*, 337–342.

Opitz, C.A., Litzenburger, U.M., Sahm, F., Ott, M., Tritschler, I., Trump, S., Schumacher, T., Jestaedt, L., Schrenk, D., Weller, M., et al. (2011). An endogenous tumour-promoting ligand of the human aryl hydrocarbon receptor. Nature *478*, 197–203.

Petersen, S.L., Peyton, M., Minna, J.D., and Wang, X. (2010). Overcoming cancer cell resistance to Smac mimetic induced apoptosis by modulating cIAP-2 expression. Proc. Natl. Acad. Sci. USA *107*, 11936–11941.

Pierini, R., Juruj, C., Perret, M., Jones, C.L., Mangeot, P., Weiss, D.S., and Henry, T. (2012). AIM2/ASC triggers caspase-8-dependent apoptosis in Francisella-infected caspase-1-deficient macrophages. Cell Death Differ. *19*, 1709–1721.

Prat, A., Parker, J.S., Karginova, O., Fan, C., Livasy, C., Herschkowitz, J.I., He, X., and Perou, C.M. (2010). Phenotypic and molecular characterization of the claudin-low intrinsic subtype of breast cancer. Breast Cancer Res. *12*, R68.

Razi, M., Chan, E.Y., and Tooze, S.A. (2009). Early endosomes and endosomal coatomer are required for autophagy. J. Cell Biol. *185*, 305–321.

Safa, A.R., and Pollok, K.E. (2011). Targeting the anti-apoptotic protein c-FLIP for cancer therapy. Cancers (Basel) *3*, 1639–1671.

Sagulenko, V., Thygesen, S.J., Sester, D.P., Idris, A., Cridland, J.A., Vajjhala, P.R., Roberts, T.L., Schroder, K., Vince, J.E., Hill, J.M., et al. (2013). AIM2 and NLRP3 inflammasomes activate both apoptotic and pyroptotic death pathways via ASC. Cell Death Differ. *20*, 1149–1160.

Sharma, S.V., Haber, D.A., and Settleman, J. (2010). Cell line-based platforms to evaluate the therapeutic efficacy of candidate anticancer agents. Nat. Rev. Cancer *10*, 241–253.

Soda, M., Choi, Y.L., Enomoto, M., Takada, S., Yamashita, Y., Ishikawa, S., Fujiwara, S., Watanabe, H., Kurashina, K., Hatanaka, H., et al. (2007). Identification of the transforming EML4-ALK fusion gene in non-small-cell lung cancer. Nature *448*, 561–566.

Son, J., Lyssiotis, C.A., Ying, H., Wang, X., Hua, S., Ligorio, M., Perera, R.M., Ferrone, C.R., Mullarky, E., Shyh-Chang, N., et al. (2013). Glutamine supports pancreatic cancer growth through a KRAS-regulated metabolic pathway. Nature *496*, 101–105.

Strowig, T., Henao-Mejia, J., Elinav, E., and Flavell, R. (2012). Inflammasomes in health and disease. Nature *481*, 278–286.

Tenev, T., Bianchi, K., Darding, M., Broemer, M., Langlais, C., Wallberg, F., Zachariou, A., Lopez, J., MacFarlane, M., Cain, K., and Meier, P. (2011). The Ripoptosome, a signaling platform that assembles in response to genotoxic stress and loss of IAPs. Mol. Cell *43*, 432–448.

Tschopp, J., Irmler, M., and Thome, M. (1998). Inhibition of fas death signals by FLIPs. Curr. Opin. Immunol. *10*, 552–558.

Wathelet, M.G., Clauss, I.M., Content, J., and Huez, G.A. (1988). The IFI-56K and IFI-54K interferon-inducible human genes belong to the same gene family. FEBS Lett. *231*, 164–171.

Wu, W.J., Erickson, J.W., Lin, R., and Cerione, R.A. (2000). The gamma-subunit of the coatomer complex binds Cdc42 to mediate transformation. Nature *405*, 800–804.

Young, R.M., Ackerman, D., Quinn, Z.L., Mancuso, A., Gruber, M., Liu, L., Giannoukos, D.N., Bobrovnikova-Marjon, E., Diehl, J.A., Keith, B., and Simon, M.C. (2013). Dysregulated mTORC1 renders cells critically dependent on desaturated lipids for survival under tumor-like stress. Genes Dev. *27*, 1115–1131.

Zhao, L., Yue, P., Lonial, S., Khuri, F.R., and Sun, S.Y. (2011). The NEDD8-activating enzyme inhibitor, MLN4924, cooperates with TRAIL to augment apoptosis through facilitating c-FLIP degradation in head and neck cancer cells. Mol. Cancer Ther. *10*, 2415–2425.